JOURNAL OF AIRCRAFT
Vol. 39, No. 5, September–October 2002

Improved Method for Rotor Wake Capturing

Haedong Kim,* Marc H. Williams,† and Anastasios S. Lyrintzis‡
Purdue University, West Lafayette, Indiana 47907

An accurate simulation of rotor aerodynamics has been a challenging problem for the computational fluid dynamics community, largely because numerical diffusion in the typically coarse grids away from the blades seriously degrades the prediction of the returning wakes. A numerical scheme is proposed to improve the reconstruction stage of a MUSCL approach in the framework of a finite volume formulation. A fourth-order upwind scheme, based on the interpolation of the local characteristic variables in the reconstruction stage, is applied instead of the conventional third-order upwind-biased scheme. Different slope limiters are applied to different characteristic fields to reduce the numerical dissipation of entropy and shear waves. We have implemented the proposed scheme into the TURNS code. Numerical results for a hover case show a significant improvement in the wake capturing capability over the baseline TURNS code.

Nomenclature

c	=	wave speed
M_{tip}	=	tip Mach number
$\hat{\boldsymbol{n}}$	=	unit vector normal to cell interface, $n_x\hat{i} + n_y\hat{j} + n_z\hat{k}$
p	=	pressure
t	=	time
u, v, w	=	velocity components in Cartesian coordinates
x, y, z	=	Cartesian coordinates
γ	=	ratio of specific heats
Δ	=	difference
δ	=	variation
ρ	=	density of air
Ψ	=	azimuth angle
Ω	=	angular velocity in the z direction for the rotor blade

Introduction

UNLIKE fixed-wing aircraft, rotorcraft create an unsteady vortical wake near the rotor disk that induces strong downwash and changes the effective angle of attack of the rotor. The tip vortex shed from the preceding blades interacts with the following blades, usually during maneuvers or in vertical descent and landing flight. This so-called blade/vortex interaction (BVI) is a major source of aerodynamic noise and structural vibration.

To design an efficient and quiet helicopter, it is crucial to analyze the complex rotor flowfield accurately and efficiently. However, in spite of huge advances in computer hardware and numerical algorithms, an accurate numerical simulation of rotor wake flow is one of the most challenging problems in rotor computational fluid dynamics (CFD). One of primary deficiencies of the current CFD codes is their inability to resolve the vortical wake adequately, without impractically fine grids. The numerically predicted vorticity diffuses rapidly due to numerical dissipation. Thus, the tip vortices can not be convected long enough to obtain accurate predictions for rotor air load and noise. An obvious way to reduce the effect of numerical diffusion for vortex flows is to increase the order of accuracy of the scheme because the leading dissipation term in the truncation error of the scheme will be dropped. In addition, the use of a higher-order scheme relaxes the grid density requirements to enable accurate predictions.

The TURNS code developed by Srinivasan et al.[1] is an Euler/Navier–Stokes solver based on first principles, without any need for external wake models. Although the TURNS code is considered as one of the best available rotor flowfield analysis codes, it has been shown that the numerical diffusion is too excessive to capture the vortex wake properly to simulate a self-generated BVI, or even hovering performance, accurately.[2] In an effort to reduce numerical diffusion in the TURNS code, various approaches have been tried recently. Wang et al.[3] implemented Nance's low-dispersion finite volume (LDFV) ideas[4] into the TURNS code and solved for rotor noise and hovering performance of Caradonna and Tung's model rotor.[5] Usta et al.[6] implemented the Yee et al. symmetric total variation diminishing[7] into the TURNS code and studied model helicopter rotor shock noise. Tang and Baeder[8] modified TURNS by introducing a monotonicity preserving piecewise quadratic reconstruction and grid redistribution technique and simulated a hovering rotor flow. The aforementioned approaches have had different degrees of success, but there is still room for improvement.

In this paper, the fourth-order MUSCL total variation diminishing scheme developed by Yamamoto and Daiguji,[9] and a characteristic-based reconstruction using different slope limiters on different characteristic fields, as in Refs. 10 and 11, are applied to the TURNS code. The test problem is the hovering rotor of Caradonna and Tung.[5]

Mathematical and Numerical Formulations

Governing Equations

The governing differential equations are the unsteady, three-dimensional equations of a compressible, inviscid flow, that is, the Euler equations. The conservation form of the three-dimensional Euler equations can be written in the rotational frame as

$$\frac{\partial \boldsymbol{Q}}{\partial t} + \frac{\partial \boldsymbol{E}}{\partial x} + \frac{\partial \boldsymbol{F}}{\partial y} + \frac{\partial \boldsymbol{G}}{\partial z} = \boldsymbol{S} \tag{1}$$

where $\boldsymbol{Q}$ represents the vector of conservative variables of the flow and $\boldsymbol{E}$, $\boldsymbol{F}$, and $\boldsymbol{G}$ are inviscid flux vectors. The source term $\boldsymbol{S}$ in the right side of the equation equals $[0, \Omega\rho v, -\Omega\rho u, 0, 0]^T$, which accounts for the centrifugal force of rotation of the blade in the x–y plane.

The restriction to inviscid flow is not necessary; Navier–Stokes calculations could as easily be done. However, the essential issue to be addressed here, capturing of wake structures that cannot be resolved by the grid, is most clearly examined in inviscid flow (where

Received 15 August 2001; revision received 10 July 2002; accepted for publication 20 July 2002.

*Graduate Student, School of Aeronautics and Astronautics. Member AIAA.
†Professor and Associate Head, School of Aeronautics and Astronautics. Member AIAA.
‡Professor, School of Aeronautics and Astronautics. Associate Fellow AIAA.

the wakes are in principle discontinuities and thickness derives only from numerical dissipation.)

Spatial Discretization in Finite Volume Formulation

The governing equations in differential form can be written in integral form for an arbitrary region V with its boundary S as

$$\frac{\partial}{\partial t}\int_V \boldsymbol{Q}\,\mathrm{d}V + \oint_S \boldsymbol{F}\cdot\hat{\boldsymbol{n}}\,\mathrm{d}S = \int_V \boldsymbol{S}\,\mathrm{d}V \tag{2}$$

where $\boldsymbol{F} = \boldsymbol{E}\hat{i} + \boldsymbol{F}\hat{j} + \boldsymbol{G}\hat{k}$ and $\hat{\boldsymbol{n}}$ denotes the outward normal vector of the control surface.

By application of the integral form of the conservation laws to a discrete cell element $V_{i,j,k}$, and by the use of the midpoint rule, they can be written as

$$\frac{\partial}{\partial t}(\boldsymbol{Q}_{i,j,k}V_{i,j,k}) + \sum_l \boldsymbol{F}_l\cdot\hat{\boldsymbol{n}}_l\Delta S_l = \boldsymbol{S}_{i,j,k}V_{i,j,k} \tag{3}$$

where the index l associated with the flux terms refers to the external side of the control volume $V_{i,j,k}$ and $\boldsymbol{Q}_{i,j,k}$ is a cell-averaged conservative variables vector of the control volume.

The design principle for the construction of the numerical flux function $\boldsymbol{F}_l$ determines the characteristics and order of spatial accuracy of the scheme. The inviscid fluxes are evaluated by Roe's numerical flux function,[12] and the high-order spatial accuracy is achieved by the use of the van Leer's MUSCL approach. In the present study, the MUSCL-type interpolation is carried out via primitive variables or local characteristic variables as proposed by Yee.[13]

The numerical algorithm used in the TURNS code is a third-order MUSCL upwind-biased finite difference scheme with Roe's numerical flux[12] and the lower–upper symmetric gauss–Seidel implicit solver. For a computation of hovering flowfield, a local time-stepping technique is used to accelerate convergence to the steady-state solution.

Third-Order MUSCL Upwind Scheme

The variables $\boldsymbol{q}^L$ and $\boldsymbol{q}^R$ interpolated at the cell interface $(i+\frac{1}{2})$ are reconstructed as

$$\begin{aligned}\boldsymbol{q}^L_{i+\frac{1}{2}} &= \boldsymbol{q}_i + \tfrac{1}{6}\Delta\bar{\boldsymbol{q}}_{i-\frac{1}{2}} + \tfrac{1}{3}\Delta\tilde{\boldsymbol{q}}_{i+\frac{1}{2}}\\ \boldsymbol{q}^R_{i+\frac{1}{2}} &= \boldsymbol{q}_{i+1} - \tfrac{1}{3}\Delta\bar{\boldsymbol{q}}_{i+\frac{1}{2}} - \tfrac{1}{6}\Delta\tilde{\boldsymbol{q}}_{i+\frac{3}{2}}\end{aligned} \tag{4}$$

where

$$\begin{aligned}\Delta\bar{\boldsymbol{q}}_{i-\frac{1}{2}} &= \Phi\left(\Delta\boldsymbol{q}_{i-\frac{1}{2}}, \Delta\boldsymbol{q}_{i+\frac{1}{2}}\right)\\ \Delta\tilde{\boldsymbol{q}}_{i+\frac{1}{2}} &= \Phi\left(\Delta\boldsymbol{q}_{i+\frac{1}{2}}, \Delta\boldsymbol{q}_{i-\frac{1}{2}}\right)\\ \Delta\bar{\boldsymbol{q}}_{i+\frac{1}{2}} &= \Phi\left(\Delta\boldsymbol{q}_{i+\frac{1}{2}}, \Delta\boldsymbol{q}_{i+\frac{3}{2}}\right)\\ \Delta\tilde{\boldsymbol{q}}_{i+\frac{3}{2}} &= \Phi\left(\Delta\boldsymbol{q}_{i+\frac{3}{2}}, \Delta\boldsymbol{q}_{i+\frac{1}{2}}\right)\end{aligned} \tag{5}$$

$$\Delta\boldsymbol{q}_{i+\frac{1}{2}} = \boldsymbol{q}_{i+1} - \boldsymbol{q}_i \tag{6}$$

Φ is a slope limiter that will be explained later. Note that the $\boldsymbol{q}$ vector denotes either primitive or characteristic variables in the present study.

Fourth-Order MUSCL Upwind Scheme

The fourth-order MUSCL scheme developed by Yamamoto and Daiguji[9] is used in the reconstruction stage in this study. The variables $\boldsymbol{q}^L$ and $\boldsymbol{q}^R$ interpolated at the cell interface $(i+\frac{1}{2})$ are reconstructed as:

$$\begin{aligned}\boldsymbol{q}^L_{i+\frac{1}{2}} &= \boldsymbol{q}_i + \tfrac{1}{6}\Delta^*\bar{\boldsymbol{q}}_{i-\frac{1}{2}} + \tfrac{1}{3}\Delta^*\tilde{\boldsymbol{q}}_{i+\frac{1}{2}}\\ \boldsymbol{q}^R_{i+\frac{1}{2}} &= \boldsymbol{q}_{i+1} - \tfrac{1}{3}\Delta^*\bar{\boldsymbol{q}}_{i+\frac{1}{2}} - \tfrac{1}{6}\Delta^*\tilde{\boldsymbol{q}}_{i+\frac{3}{2}}\end{aligned} \tag{7}$$

where

$$\begin{aligned}\Delta^*\bar{\boldsymbol{q}}_{i-\frac{1}{2}} &= \Phi\left(\Delta^*\boldsymbol{q}_{i-\frac{1}{2}}, \Delta^*\boldsymbol{q}_{i+\frac{1}{2}}\right)\\ \Delta^*\tilde{\boldsymbol{q}}_{i+\frac{1}{2}} &= \Phi\left(\Delta^*\boldsymbol{q}_{i+\frac{1}{2}}, \Delta^*\boldsymbol{q}_{i-\frac{1}{2}}\right)\\ \Delta^*\bar{\boldsymbol{q}}_{i+\frac{1}{2}} &= \Phi\left(\Delta^*\boldsymbol{q}_{i+\frac{1}{2}}, \Delta^*\boldsymbol{q}_{i+\frac{3}{2}}\right)\\ \Delta^*\tilde{\boldsymbol{q}}_{i+\frac{3}{2}} &= \Phi\left(\Delta^*\boldsymbol{q}_{i+\frac{3}{2}}, \Delta^*\boldsymbol{q}_{i+\frac{1}{2}}\right)\end{aligned} \tag{8}$$

$$\Delta^*\boldsymbol{q}_{i+\frac{1}{2}} = \Delta\boldsymbol{q}_{i+\frac{1}{2}} - \tfrac{1}{6}\Delta^3\bar{\boldsymbol{q}}_{i+\frac{1}{2}} \tag{9}$$

$$\Delta^3\bar{\boldsymbol{q}}_{i+\frac{1}{2}} = \Delta\bar{\boldsymbol{q}}_{i-\frac{1}{2}} - 2\Delta\bar{\boldsymbol{q}}_{i+\frac{1}{2}} + \Delta\bar{\boldsymbol{q}}_{i+\frac{3}{2}} \tag{10}$$

with

$$\begin{aligned}\Delta\bar{\boldsymbol{q}}_{i-\frac{1}{2}} &= \mathrm{minmod}\left(\Delta\boldsymbol{q}_{j-\frac{1}{2}}, b\Delta\boldsymbol{q}_{j+\frac{1}{2}}, b\Delta\boldsymbol{q}_{j+\frac{3}{2}}\right)\\ \Delta\bar{\boldsymbol{q}}_{i+\frac{1}{2}} &= \mathrm{minmod}\left(\Delta\boldsymbol{q}_{j+\frac{1}{2}}, b\Delta\boldsymbol{q}_{j+\frac{3}{2}}, b\Delta\boldsymbol{q}_{j-\frac{1}{2}}\right)\\ \Delta\bar{\boldsymbol{q}}_{i+\frac{3}{2}} &= \mathrm{minmod}\left(\Delta\boldsymbol{q}_{j+\frac{3}{2}}, b\Delta\boldsymbol{q}_{j-\frac{1}{2}}, b\Delta\boldsymbol{q}_{j+\frac{1}{2}}\right)\end{aligned} \tag{11}$$

$$\begin{aligned}&\mathrm{minmod}(x, y, z)\\ &\quad = \mathrm{sign}(x)\max\{0.0, \min[|x|, y\,\mathrm{sign}(x), z\,\mathrm{sign}(x)]\}\end{aligned} \tag{12}$$

$$1 < b \le 4 \tag{13}$$

These forms are quite similar to those of the third-order MUSCL scheme. Only $\Delta\boldsymbol{q}$ in Eq. (5) is replaced by $\Delta^*\boldsymbol{q}$ in Eq. (8). $\Delta^*\boldsymbol{q}$ is composed of two terms, that is, the ordinary third-order term and a fourth-order correction term. First, a slope limiter is applied to the latter term, like Eq. (11). In this limiter function, three neighboring slopes $\Delta\boldsymbol{q}$ are compared with each other, and, if the sign of any slope is different from the others, then the fourth-order correction term is removed. The value b in the Eq. (13) is specified as $b=2$ in this study. Next, the slopes in Eq. (8), in which the value $\Delta^3\bar{\boldsymbol{q}}$ is calculated by Eq. (10), are further limited by using slope limiters, as will be explained later. Different slope limiters are applied to different characteristic fields in this study. Thus, a discussion of characteristic decomposition and slope limiters follows.

Characteristic Decomposition

A system of conservation laws, such as the Euler equations, can be best understood by transforming them to local characteristic variables that display largely decoupled scalar behavior. The characteristic variables are defined by multiplication of the primitive variable vector by a set of the left eigenvectors of the flux Jacobian matrix.[11] For example, the variations of the characteristic variables in the two-dimensional case are

$$\begin{aligned}\delta w_1 &= \delta\rho - (1/c^2)\delta p, \qquad & \delta w_2 &= n_y\delta u - n_x\delta v\\ \delta w_3 &= \hat{n}\cdot\delta\boldsymbol{v} + \delta p/\rho c, \qquad & \delta w_4 &= -\hat{n}\cdot\delta\boldsymbol{v} + \delta p/\rho c\end{aligned} \tag{14}$$

The first two characteristic variables associated with the entropy perturbation and vorticity wave, respectively, are a linearly degenerate field that dissipates in the presence of numerical diffusion (wave speed is indepenent of amplitude). The last two characteristic variables associated with acoustic pressure waves are a nonlinear field that has a self-stiffening mechanism (wave speed depends on amplitude).[14] In this study, the characteristic variable differences are obtained as follows:

$$\Delta\boldsymbol{W} = \boldsymbol{L}\Delta\boldsymbol{Q} \tag{15}$$

where $\boldsymbol{W}$ is a characteristic variables vector and $\boldsymbol{L}$ is a set of left eigenvectors of the flux Jacobian matrix. The local characteristic

variables at interface $(i + \frac{1}{2})$ are determined by (indices j and k are omitted for clarity):

$$\boldsymbol{W}^L_{i+\frac{1}{2}} = \boldsymbol{Q}_i + \boldsymbol{L}\big(\boldsymbol{Q}_i, \hat{n}_{i+\frac{1}{2}}\big)\chi^{(L)}(\boldsymbol{Q}_{i+m})$$

$$\boldsymbol{W}^R_{i+\frac{1}{2}} = \boldsymbol{Q}_{i+1} - \boldsymbol{L}\big(\boldsymbol{Q}_{i+1}, \hat{n}_{i+\frac{1}{2}}\big)\chi^{(R)}(\boldsymbol{Q}_{i+1+m}) \qquad (16)$$

where

$$m = \begin{cases} -1, 0, 1 & \text{for third-order MUSCL} \\ -2, -1, 0, 1, 2 & \text{for fourth-order MUSCL} \end{cases}$$

In Eq. (16) $\chi^{(L)}$ and $\chi^{(R)}$ are interpolation functions used in the MUSCL approach. Note that $\boldsymbol{L}$ in the preceding expression is frozen at $\boldsymbol{Q}_i$ for $\boldsymbol{W}^L_{i+1/2}$ and at $\boldsymbol{Q}_{i+1}$ for $\boldsymbol{W}^R_{i+1/2}$, respectively. The corresponding conservative variables $\boldsymbol{Q}^L_{i+1/2}$ and $\boldsymbol{Q}^R_{i+1/2}$ are calculated by

$$\boldsymbol{Q}^L_{i+\frac{1}{2}} = \boldsymbol{R}\big(\boldsymbol{Q}_i, \hat{n}_{i+\frac{1}{2}}\big)\boldsymbol{W}^L_{i+\frac{1}{2}}$$

$$\boldsymbol{Q}^R_{i+\frac{1}{2}} = \boldsymbol{R}\big(\boldsymbol{Q}_{i+1}, \hat{n}_{i+\frac{1}{2}}\big)\boldsymbol{W}^R_{i+\frac{1}{2}} \qquad (17)$$

where $\boldsymbol{R} = \boldsymbol{L}^{-1}$ is a set of right eigenvectors of the flux Jacobian matrix.

Slope Limiters

The limiter functions used in the MUSCL interpolation are as follows:

1) The minmod limiter[15] is

$$\Phi^{(mn)}(a, \beta b) = \text{sign}(a)\max\{0, \min[\beta b\,\text{sign}(a), |a|]\} \qquad (18)$$

where β is a compression parameter.

2) Roe's Superbee limiter[15] is

$$\Phi^{(SB)}(a, b) = \text{sign}(a)\max\{0, \min[2|a|, \text{sign}(a)b], \min[|a|, 2\text{sign}(a)b]\} \qquad (19)$$

Unlike the nonlinear characteristic fields, the linear characteristic fields do not have a self-stiffening mechanism.[16] Therefore, the compressive limiters (like Roe's Superbee[15]) are applied to the linear fields, whereas the diffusive limiters (like minmod) are used for the nonlinear fields to suppress spurious numerical oscillations following Sweby[10] and Yee.[13]

Results and Discussion

Several model problems, including two-dimensional vortex convection, were studied to test the accuracy and wake capturing capability of the proposed scheme. Computational results suggest that the proposed scheme preserve a convecting unresolved (i.e., having only a couple of points in the core) vortex better than the conventional third-order MUSCL scheme in TURNS. These results can be found in Ref. 17 and will not be reproduced here. However, they did provide the motivation for the application to TURNS, which is reported here.

We have performed an Euler simulation of a hovering rotor flow using the basic TURNS code and modifications of it. The presented numerical results are mainly focused on the improvement of the vortex capturing capability of the proposed scheme.

The Euler calculation of Caradonna and Tung's rotor[5] in hover was performed by the baseline TURNS code and the modified TURNS code based on the proposed fourth-order MUSCL upwind scheme with characteristic decomposition. The blade is untwisted and has a rectangular planform with NACA 0012 airfoil sections and an aspect ratio of six. The computed case has a rotor collective pitch angle of 8 deg and a hovering tip Mach number equal to 0.877. Two grids are used for the present calculations. One is a relatively coarse grid, which consists of 101 points in the wraparound direction with 67 points on the body, 31 points in the spanwise direction with 21 points on the rotor surface, and 35 points in the normal direction. This gives a total of about 110,000 grid points. The other is a $211 \times 71 \times 55$ grid, as seen in Fig. 1, which is relatively fine and consists of over 820,000 grid points. The top and bottom boundaries of the grids are set at about two rotor radii above and below the rotor disk, and the outer boundaries are set at 1.8 rotor radii in all directions.

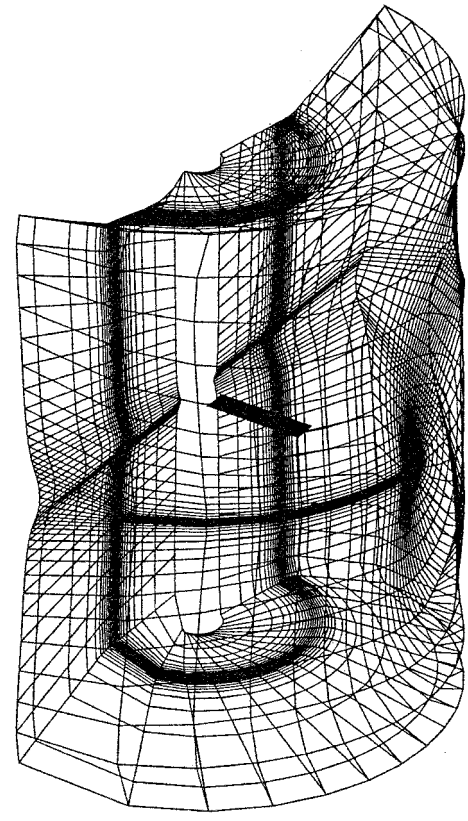

Fig. 1 Fine grid used for the computation (every third point is shown).

Four types of boundary conditions are used for the calculation of the flowfield around a hovering rotor: 1) a solid wall boundary condition, 2) a periodic boundary condition, 3) a far-field boundary condition, and 4) an inboard boundary condition. All of the boundary conditions are applied explicitly. The details of the boundary conditions used for the present study are presented in Ref. 1.

The convergence to steady state is determined by monitoring the thrust coefficient history. This usually required about 10,000 iterations for the coarse grid and about 25,000 iterations for the fine grid. For the fine grid, the computation of the baseline TURNS required about 50 h of CPU time on the Ultra 450 of Sun Microsystems. Compared to the baseline TURNS, the CPU time is increased by about 10% with the implementation of the fourth-order MUSCL upwind interpolation and by about 40% with the implementation of the fourth-order MUSCL upwind interpolation of characteristic variables with the application of different limiters on different characteristic fields. However, the proposed modifications are much cheaper than the global grid refinement needed to improve wake predictions.

Figure 2 shows the predicted and experimental pressure coefficients at five different blade sections for $M_{tip} = 0.877$ at the collective pitch angle of 8 deg. Good agreement between the computed results and experimental data are shown, except for the outboard region of the rotor blade, where the shock strength is overpredicted and the shock is located farther downstream. This discrepancy is because the present calculations are inviscid. Viscous effects, like shock/boundary-layer interaction, tend to make the shock weaken

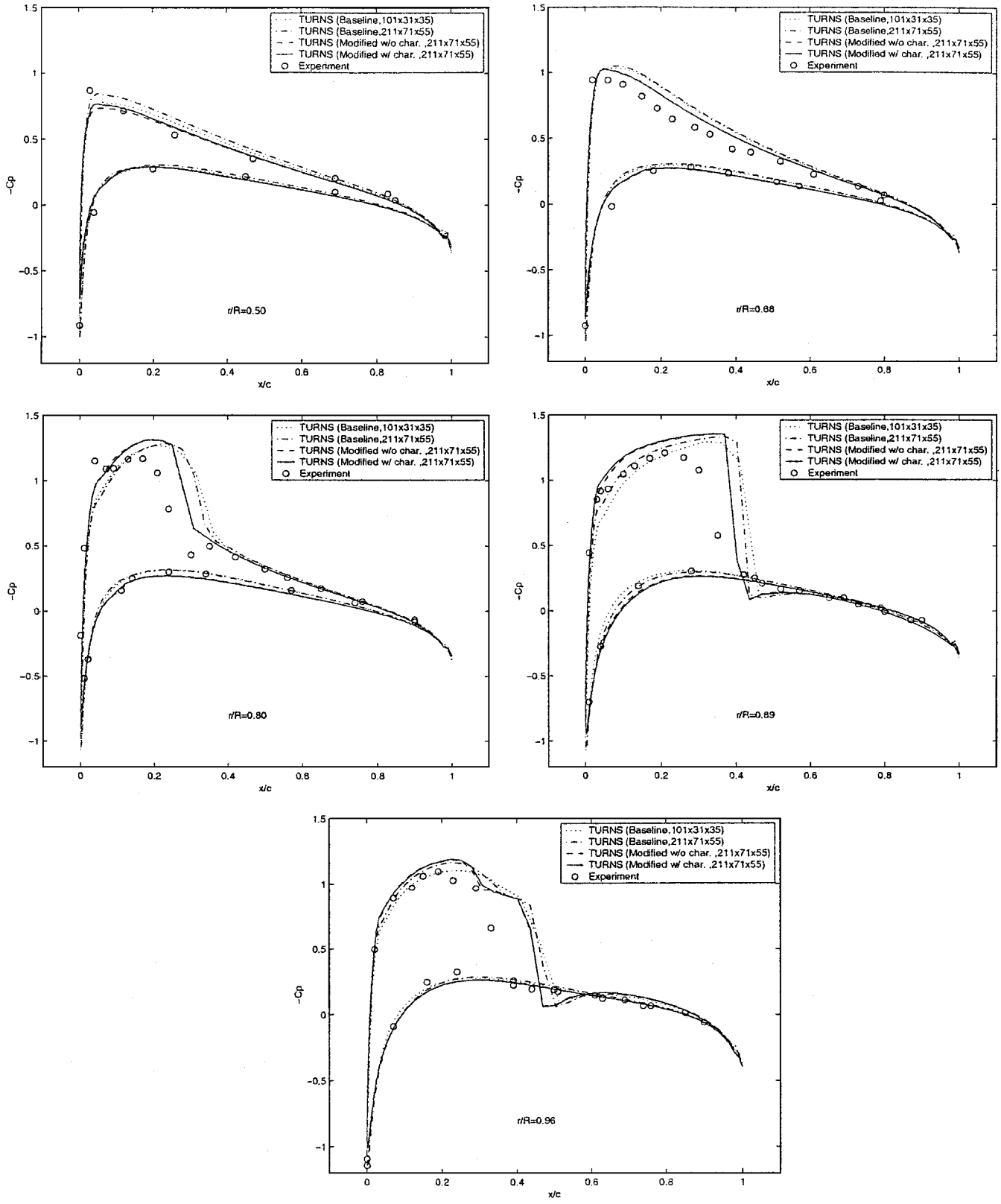

Fig. 2 Surface pressure coefficients at Mach = 0.877 and collective pitch angle of 8 deg.

and move toward the leading edge. There is no remarkable difference between the computed results on the coarse grid and on the fine grid, except that the pressure peak near the leading edge is increased and a sharper shock is captured on the fine grid because of increased grid density. However, the difference between the shock locations from baseline and modified TURNS are noticeable. The modified schemes predict shock location closer to the leading edge by two or three cells, compared to the baseline TURNS prediction. It appears that the higher-order discretization plays an important role in capturing a shock wave in the proper location. However, the use of the selective application of different limiters to different characteristic fields does not appear to make a significant difference in shock capturing for this steady transonic flow. Overall, present predictions of the surface pressure on the rotor blade show reasonably good agreements with the experimental data, except that they overpredict pressure coefficients on the leading-edge suction side of the rotor

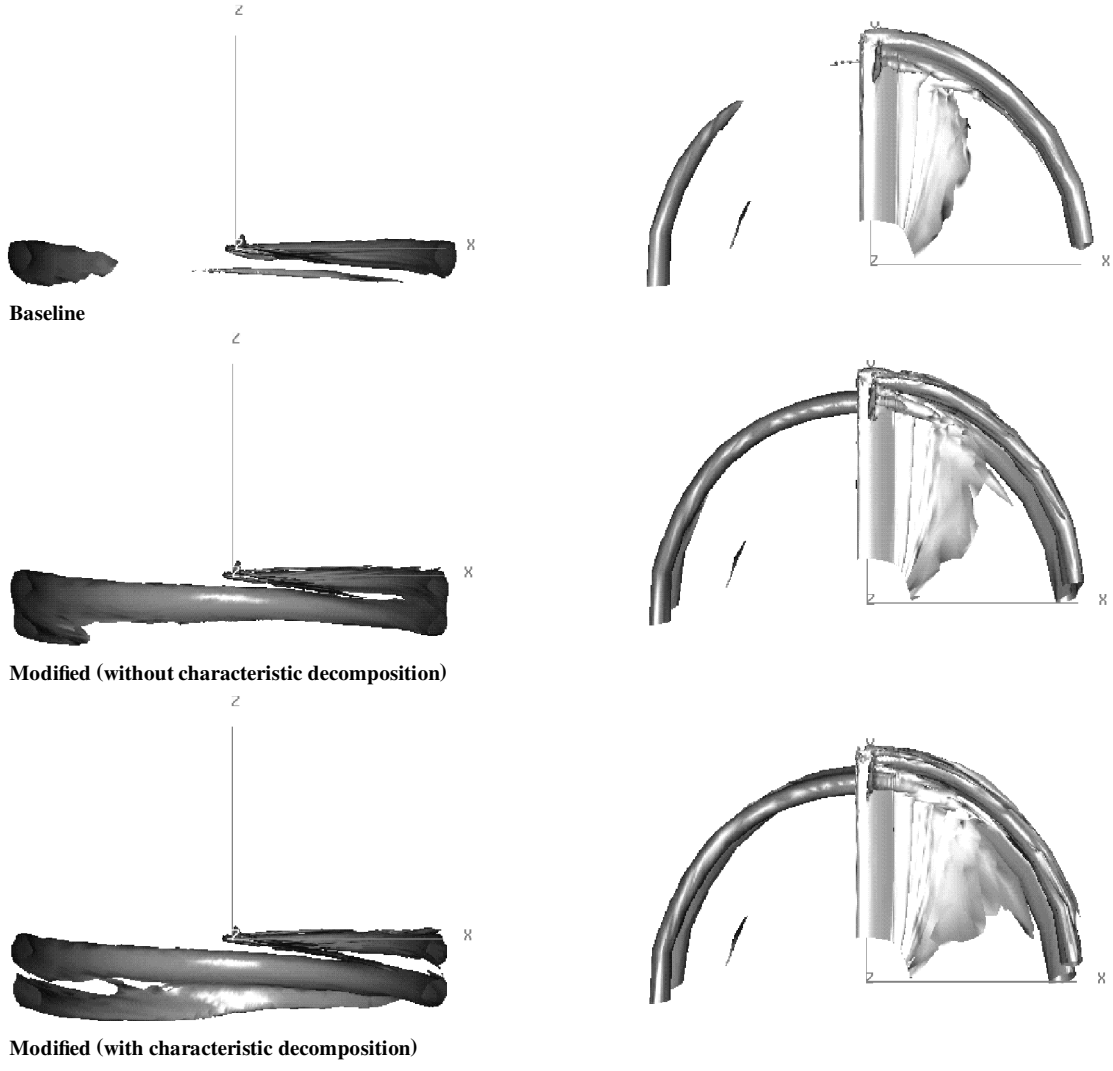

Fig. 3 Comparison between baseline TURNS code and modifications for the coarse grid (isovorticity magnitude surface of value = 0.2).

blade and the shock strength. This is probably because the inviscid model is used.

Figures 3 and 4 show the side and top views of an isovorticity magnitude surface value equal to 0.2, predicted by the baseline and the modified TURNS codes on a coarse and a fine grid, respectively. Only one-half of the wake is shown due to symmetry. Apparently, the modified TURNS codes, especially the fourth-order MUSCL upwind scheme with the selective application of different limiters to different characteristic fields, capture the vortex wake better than the baseline TURNS code. The rotor tip vortex is preserved further downstream both on the coarse and fine grids. Both grid density and the interpolation method influence the results noticeably. An increased grid density provides a more detailed rotor wake system with tightly braided rotor tip vortices and preserves them for a longer distance, as expected. Also, the order of accuracy of the interpolation plays a similar role as grid density from the viewpoint of producing a more detailed rotor wake system and keeping the tip vortices from numerical diffusion for a longer distance.

Note that the additional computational cost in the higher order of MUSCL interpolation is almost negligible compared to that of the increased grid density used to obtain the same level of tip vortex preservation. The selective application of different limiters to different characteristic fields appears to improve the capability of capturing and preserving rotor tip vortices from numerical diffusion. However, it is not as effective as increasing of the spatial order of accuracy of the numerical method. It appears that the higher-order discretization plays a more important role in capturing and preserving vortex wake structures than the selective application of different limiters to different characteristic fields in rotor flow.

Figure 5 shows top and side views of an isovorticity magnitude surface value equal to 0.2, computed from the low-dispersion finite volume version of TURNS (LDFV-TURNS)[3] and the proposed method on a coarse grid. Although the LDFV-TURNS code appears to resolve the tip vortices better than the baseline TURNS, it does not do as well as the proposed scheme. Moreover, the inboard wake sheets are considerably thicker than the other numerical results. This is probably because compressive limiters (for example, Roe's Superbee[15]) are applied to primitive variables rather than characteristic variables in the reconstruction stage of the MUSCL interpolation in the LDFV-TURNS code.

Figure 6 shows the predicted vortex trajectories, along with numerical results from Refs. 18 and 19 and experimental curve fits from Ref. 5. Note that the results from Refs. 18 and 19 are from much more computationally intensive studies using embedded and solution adaptive unstructured grids, respectively. Whereas the predicted tip vortices from the modified TURNS codes on the fine grid can be tracked down to more than an azimuth angle of 400 deg, those from the baseline TURNS code on the fine grid are impossible to locate beyond an azimuth angle of 330 deg due to excessive numerical diffusion. The radial contraction of the tip vortex in Fig. 6 shows reasonably good agreement with the experimental data and other numerical results. All of the predicted vortex trajectories on the coarse grid are less contracted toward the center of rotation than those of the experimental data. It appears that the vortex has

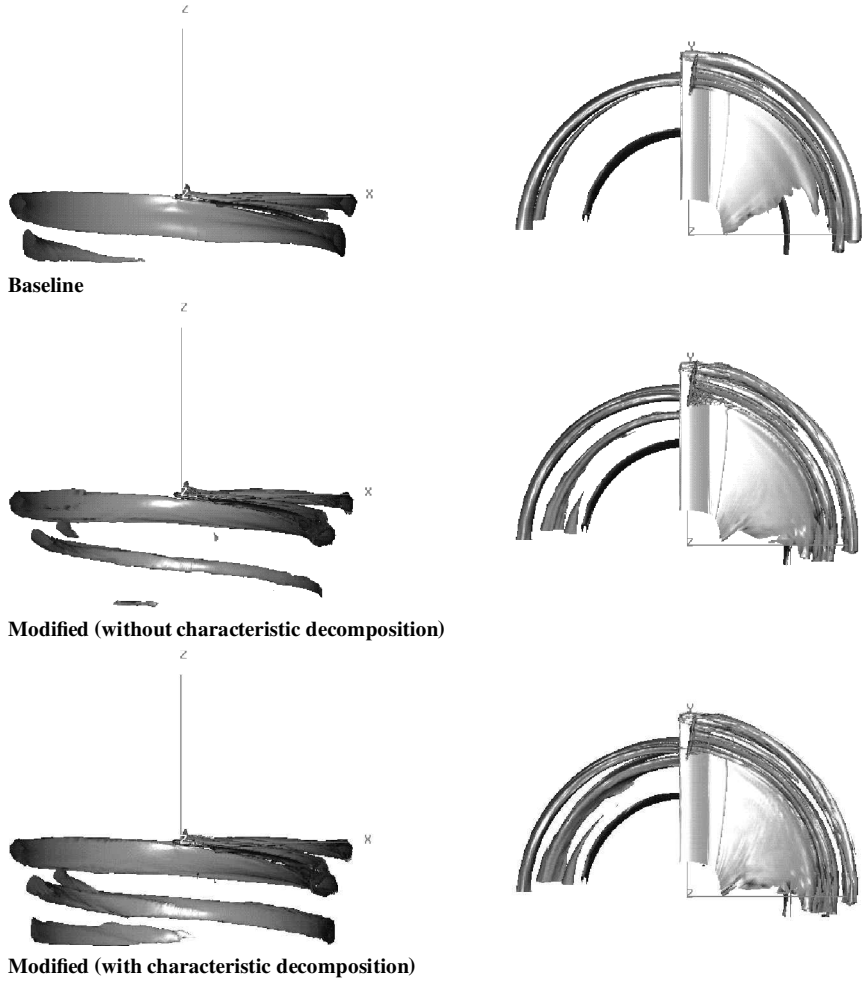

Fig. 4 Comparison between baseline TURNS code and modifications for the fine grid (isovorticity magnitude surface of value = 0.2).

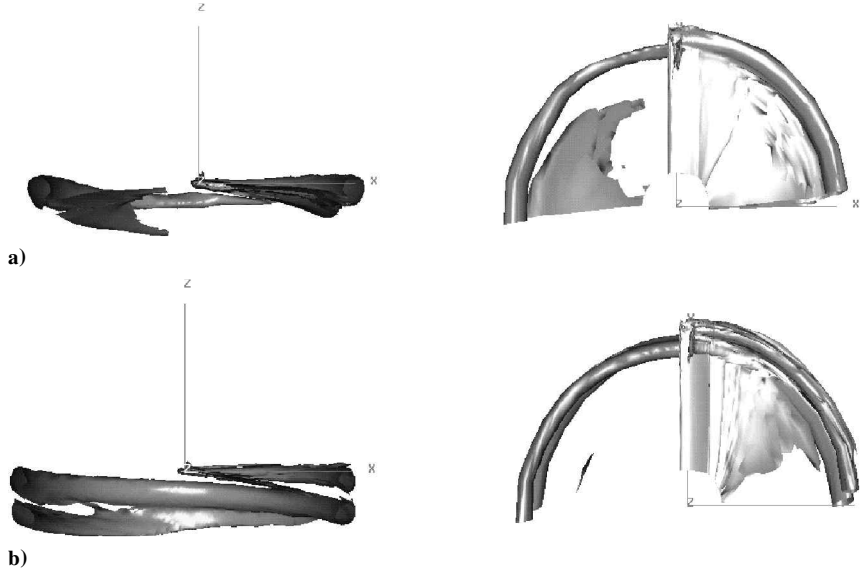

Fig. 5 Comparison between a) the LDFV-TURNS and b) the proposed method for the coarse grid (isovorticity magnitude surface of value = 0.2).

diffused significantly due to the lack of grid density. The predicted vortex trajectories from the modified TURNS codes on the fine grid are more contracted toward the center of rotation than those from the baseline TURNS code. This discrepancy in vortex trajectories probably comes from the higher spanwise surface air loads gradient near the tip region of the rotor blade (not shown here) leading to strong and tight tip vortex circulation and from its contracting the wake system more toward the center of the rotation. Finally, note that all computations (except those of Ref. 18) ignore viscous effects, which would probably increase the evaluated distances. In spite of the differences between experiment and computation for radial contraction, the computed descent of the tip vortex shows better agreement with the experimental data at azimuth angles of up to 250 deg.

Figure 7 shows vorticity magnitude contours predicted by the baseline and the modified TURNS codes on the plane 80 deg from

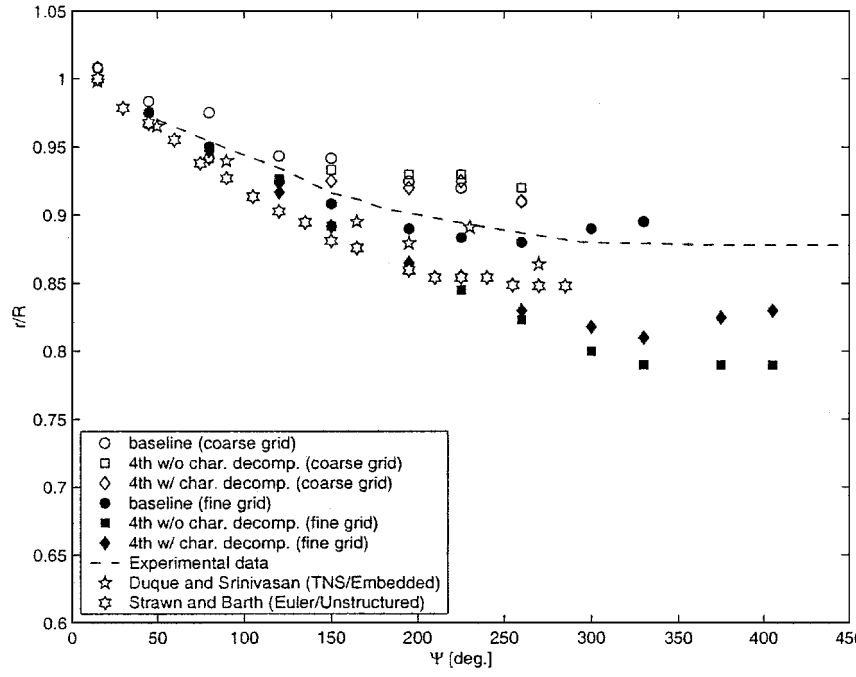

Radial location of tip vortex

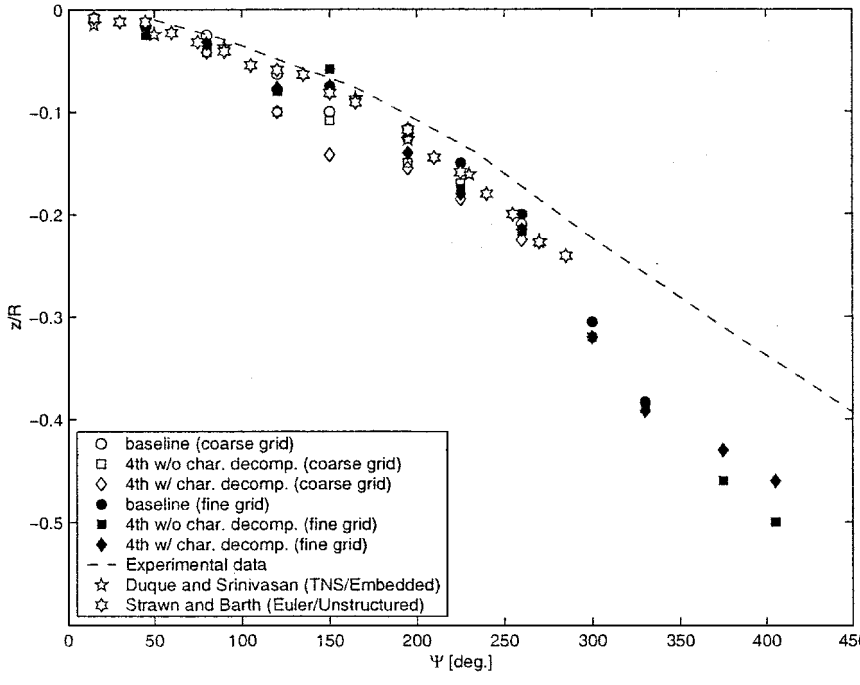

Vertical location of tip vortex

Fig. 6 Tip vortex location (8-deg collective pitch angle and M_{tip} = 0.877).

the rotor one-quarter chord line. The wake system predicted by the modified TURNS code appears clearer and with a more concentrated core than that predicted by the baseline TURNS code. Although the primary shed wake sheet and vortex are visible in all simulations, the shed wake sheet and vortex from the following blade are only seen in the fine grid modified code results. The grid refinement study demonstrated that the proposed scheme has the ability to capture and preserve the vortex wake from numerical diffusion a lot better than the baseline TURNS code. However, the detailed structure of the predicted wake system of a hovering rotor is significantly affected by the grid density. Without increasing the order of accuracy in the MUSCL interpolation, the effect of the characteristic variable reconstruction with the selective application of different limiters to different characteristic fields is beneficial for the improvement of wake capturing capability, but less dramatic than increasing the order of the MUSCL interpolation.

Another way of examining the numerical diffusion of the rotor tip vortex is by extracting induced vertical velocities across the rotor tip vortex core. Although vorticity magnitude contours are easy to visualize and suitable for a qualitative comparison of numerical diffusion between computed results, the visibility of these contour lines depends heavily on the chosen contour level sets. In addition, computed solutions are easily contaminated by numerical errors of highly stretched and skewed grids, such as the ones used for the present calculations, because the numerical differentiation of velocity is required for the vorticity field calculation. Figure 8 shows the vertical velocity profile across the tip vortex core on coarse and fine grids, respectively. It is clearly seen that the modified TURNS

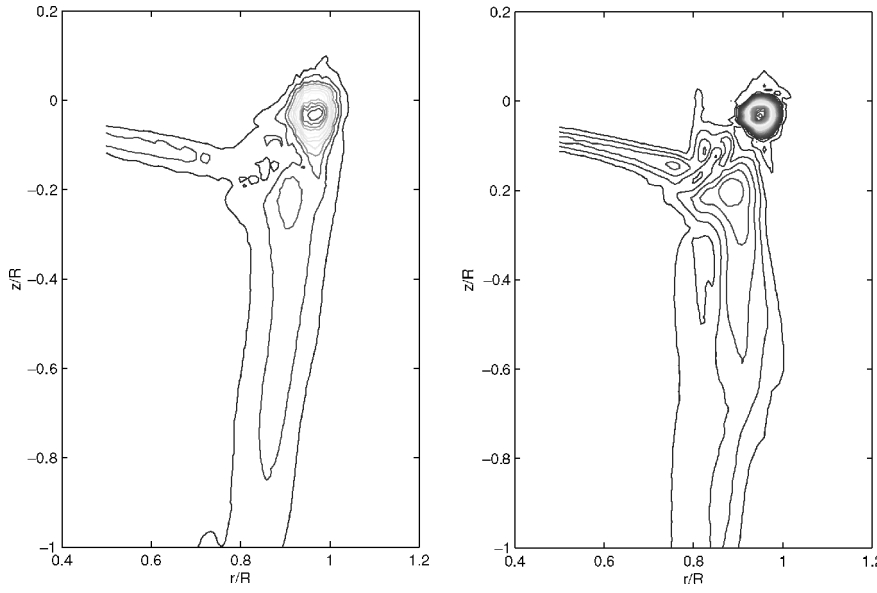

Baseline

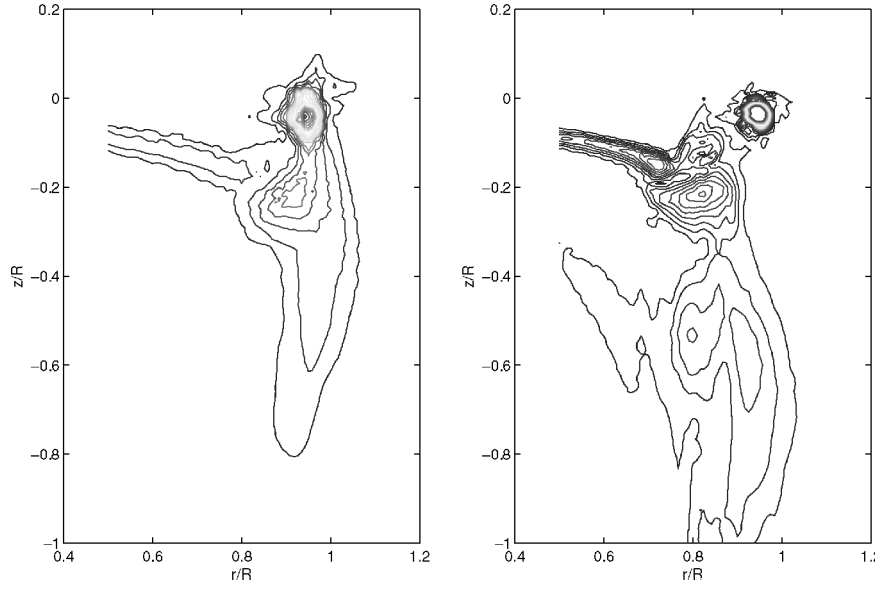

Modified (without characteristic decomposition)

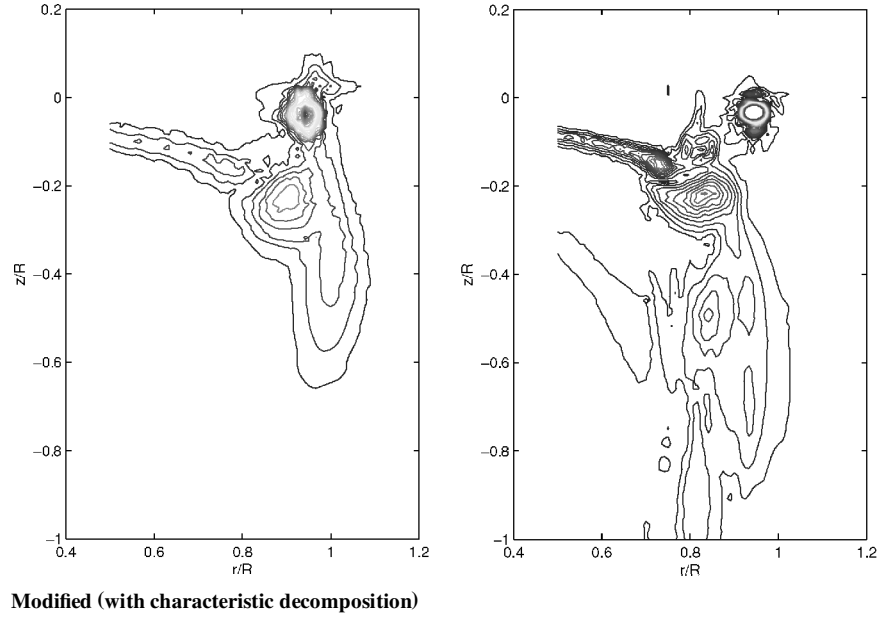

Modified (with characteristic decomposition)

Fig. 7 Vorticity contours at Ψ = 80 deg on coarse (left) and fine (right) grid, magnitude of [0:0.05:2].

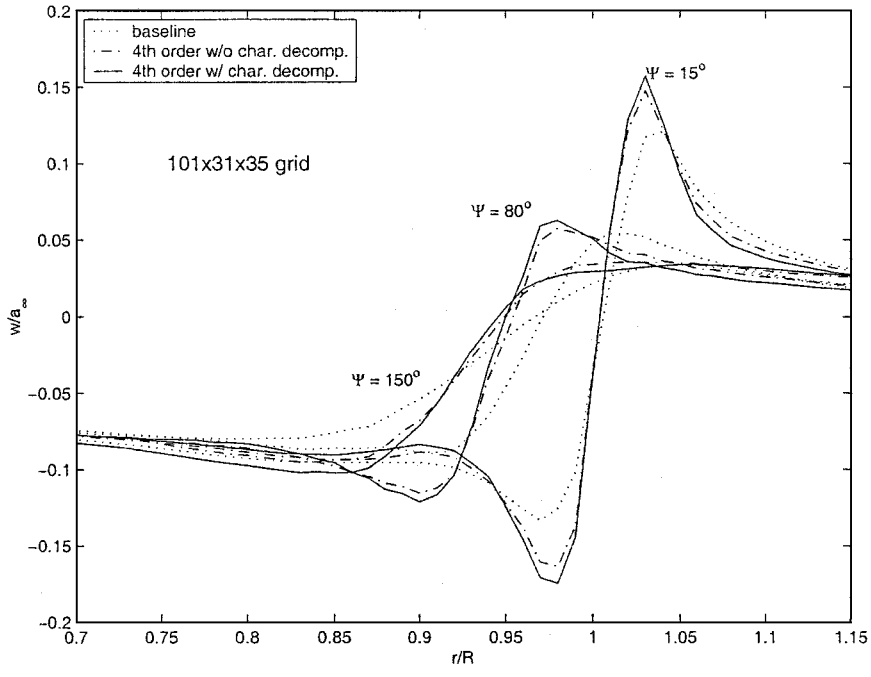

Fine grid

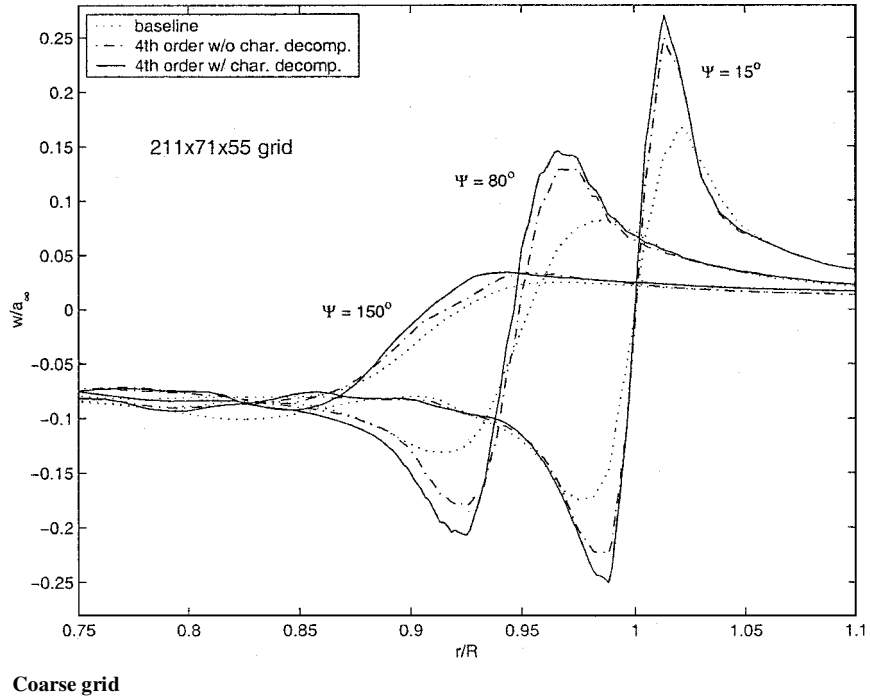

Coarse grid

Fig. 8 Vertical velocity profiles across the tip vortex core.

codes preserve the peak-to-peak induced vertical velocities better and convect them for a longer distance than the baseline TURNS code. However, the induced vertical velocities diffuse significantly after the vortex age of 90 deg due to the grid coarseness away from the rotor blade and the reduced order of accuracy in the treatment of the periodic boundary condition.

Overall, it is demonstrated that the proposed approach can capture a vortex wake system and its induced effects as part of the numerical solution without any wake model. The proposed approach can also be applied to other codes that use similar methods, for example, the well-known OVERFLOW code[20] based on overset grids.

Conclusions

A new approach is presented for improved rotor wake capturing. The fourth-order MUSCL upwind scheme proposed in Ref. 9 has been improved by the introduction of characteristic decomposition with different limiters applied to different characteristic fields in the reconstruction stage of the MUSCL interpolation. The original TURNS code was modified by using the proposed fourth-order upwind scheme and tested on the simulation of a lifting rotor in hover. Numerical results indicate that the proposed scheme has a better vortex preservation and wake-capturing capability than the traditional third-order MUSCL upwind-biased scheme. The proposed modifications can also be applied to other codes that use similar numerical methods, for example, the well-known OVERFLOW code[20] based on overset grids.

References

[1] Srinivasan, G. R., Baeder, J. D., Obayashi, S., and McCroskey, W. J., "Flowfield of a Lifting Rotor in Hover: A Navier–Stokes Simulation," *AIAA Journal*, Vol. 30, No. 10, 1992, pp. 2371–2378.

[2]Wake, B. E., and Baeder, J. D., "Evaluation of a Navier–Stokes Analysis for Hover Performance Prediction," *Journal of the American Helicopter Society*, Vol. 41, No. 1, 1996, pp. 6–17.

[3]Wang, G., Sankar, L. N., and Tadghighi, H., "Prediction of Rotorcraft Noise with a Low-Dispersion Finite Volume Scheme," *AIAA Journal*, Vol. 38, No. 3, 2000, pp. 395–401.

[4]Nance, D. V., Viswanathan, K., and Sankar, L. N., "Low-Dispersion Finite Volume Scheme for Aeroacoustic Applications," *AIAA Journal*, Vol. 35, No. 2, 1997, pp. 255–262.

[5]Caradonna, F. X., and Tung, C., "Experimental and Analytical Studies of a Model Helicopter Rotor in Hover," NASA TM 81232, 1981.

[6]Usta, E., Wang, G., and Sankar, L. N., "Application of a Symmetric Total Variation Diminishing Scheme to Shock Noise of Rotors," AIAA Paper 2000-0348, 38th Aerospace Science Meeting and Exhibit, Reno, NV, Jan. 2000.

[7]Yee, H. C., Sandham, N. D., and Djomehri, M. J., "Low Dissipative High Order Shock-Capturing Methods Using Characteristic-Based Filters," NASA CR 208237, 1998.

[8]Tang, L., and Baeder, J. D., "Improved Euler Simulation of Hovering Rotor Tip Vortices with Validation," *Proceedings of the American Helicopter Society 55th Annual Forum*, American Helicopter Society, Alexandria, VA, Vol. 2, 1999, pp. 1934–1948.

[9]Yamamoto, S., and Daiguji, S., "Higher-Order Accurate Upwind Schemes for Solving the Compressible Euler and Navier–Stokes Equations," *Computers and Fluids*, Vol. 22, No. 2/3, 1993, pp. 259–270.

[10]Sweby, P. K., "High Resolution Schemes Using Flux Limiters for Hyperbolic Conservation Laws," *SIAM Journal on Numerical Analysis*, Vol. 21, No. 5, 1984, pp. 995–1011.

[11]Hirsch, C., "Numerical Computation of Internal and External Flows, Volume 2," Wiley, New York, 1987, pp. 150–157.

[12]Roe, P. L., "Approximate Riemann Solvers, Parameter Vectors and Difference Scheme," *Journal of Computational Physics*, Vol. 43, No. 2, 1981, pp. 357–372.

[13]Yee, H. C., "Construction of Explicit and Implicit Symmetric TVD Schemes and Their Application," *Journal of Computational Physics*, Vol. 68, No. 1, 1987, pp. 151–179.

[14]Lax, P. D., "Hyperbolic Systems of Conservation Laws II," *Communications on Pure and Applied Mathematics*, Vol. 10, No. 4, 1957, pp. 537–566.

[15]Roe, P. L., "Some Contributions to the Modeling of Discontinuous Flows," *Lectures in Applied Mathematics*, Vol. 22, Pt. 2, 1985, pp. 163–193.

[16]Lax, P. D., "Weak Solution of Nonlinear Hyperbolic Equations and Their Numerical Computation," *Communications on Pure and Applied Mathematics*, Vol. 7, No. 1, 1954, pp. 159–193.

[17]Kim, H., "Computational Techniques for Blade Vortex Interaction Prediction," Ph.D. Dissertation, School of Aeronautics and Astronautics, Purdue Univ., West Lafayette, IN, Aug. 2001.

[18]Duque, E. P. N., and Srinivasan, G. R., "Numerical Simulation of a Hovering Rotor Using Embedded Grids," *Proceedings of the American Helicopter Society 48th Annual Forum*, American Helicopter Society, Alexandria, VA, Vol. 1, 1992, pp. 429–445.

[19]Strawn, R. C., and Barth, T. J., "A Finite Volume Euler Solver for Computing Rotor–Wing Aerodynamics on Unstructured Meshes," *Proceedings of the American Helicopter Society 48th Annual Forum*, American Helicopter Society, Alexandria, VA, Vol. 1, 1992, pp. 419–428.

[20]Buning, P. G., Jesperson, D.C., Pulliam, T. H., Chan, W. M., Stonick, J. P., Krist, S. E., and Renze, K. J., "OVERFLOW User's Manual, Version 1.8g," NASA Langley Research Center, Hampton, VA, March 1999.